Research Square

Preprints are preliminary reports that have not undergone peer review.
They should not be considered conclusive, used to inform clinical practice,
or referenced by the media as validated information.

Primary-to-first-rebound bubble dynamics of plasma-mediated Nd:YAG and thermally driven Er:YAG configurations in 17% EDTA solution

Yuhao Bai
Xuanwu Hospital Capital Medical University
Runjie Wei
MicroVec Ltd.
Lu Tang
Xuanwu Hospital Capital Medical University
Ying Zhao
zhaoying_a@xwh.ccmu.edu.cn

Xuanwu Hospital Capital Medical University

Research Article

Keywords: EDTA, laser-generated bubbles, plasma-mediated activation, thermally driven activation, endodontic irrigation, high-speed imaging

Posted Date: September 23rd, 2026

DOI: https://doi.org/10.21203/rs.3.rs-10921653/v1

License: This work is licensed under a Creative Commons Attribution 4.0 International License. Read Full License

Additional Declarations: No competing interests reported.

Abstract

Purpose

To characterize primary-to-first-rebound profiles of plasma-mediated Nd:YAG and thermally driven Er:YAG bubbles in unconfined 17% ethylenediaminetetraacetic acid (EDTA), emphasizing shared-setting Er:YAG mode comparisons.

Methods

Ninety independent isolated events were acquired in randomized order (nine configurations; n = 10 each). Nd:YAG laser-induced plasma activation (LIPA; 10 ns) used 100/200/300 mJ; thermally driven ultra-short-pulse (USP; 25 µs) and super-short-pulse (SSP; 50 µs) modes used 10/15/20 mJ. LIPA was not energy matched to Er:YAG. Software-exported ellipse-equivalent projected area (Size), equivalent diameter, timing and beam-referenced lengths were analysed. Ordered-setting and paired shape analyses were post hoc exploratory, with multiplicity adjustment.

Results

LIPA occupied larger absolute-size ranges under the tested configurations. At every shared Er:YAG setting, USP had larger primary/rebound projections and higher rebound/primary diameter ratios than SSP (sample Cliff's $\delta = 1.00$; adjusted $p \leq 0.0057$). SSP primary-area medians increased 41.9% from 10 to 20 mJ, whereas rebound-area medians were 1.150 and 1.139 mm²; the diameter ratio declined from 0.629 to 0.535 (adjusted trend $p = 0.000300$). Paired analysis supported transverse shifts in all USP groups and SSP10, and axial shifts in SSP20 and LIPA100/200; LIPA300 and SSP15 were not significant after adjustment.

Conclusion

Configuration-specific primary-to-rebound profiles differed across the tested initiation families and Er:YAG modes. Exploratory analysis indicated that rebound geometry was not a uniform scaling of primary geometry. These preparation-specific observations do not isolate initiation mechanisms or establish clinical efficacy.

Introduction

Ethylenediaminetetraacetic acid (EDTA) is used in endodontic irrigation to chelate the inorganic component of the smear layer and support its removal [1–4]. Solutions near 15–17% are common, although their effect on dentine depends on concentration, exposure time, and the sequence in which they are used; prolonged contact can produce surface erosion in ex vivo specimens [3, 5]. Effective delivery is therefore important. Instrumentation does not fully expose fins, isthmuses, lateral extensions, and other anatomical recesses, where residual tissue and microbial communities may persist [6–8]. Activation methods seek to improve fluid exchange in these regions, but the physical response of the irrigant remains conditional on both the activation source and the liquid being activated.

Laser-activated irrigation produces transient liquid displacement through expanding and collapsing laser-generated bubbles [9–12]. Thermally driven Er:YAG activation relies on strong absorption at 2940 nm, heating and vaporization near the delivery tip. Bubble dimensions and timing vary with pulse energy, pulse duration, repetition rate, tip geometry, insertion depth, and boundary conditions [13–19]. In canal models, the resulting dynamics have been

associated with pressure transients, irrigant exchange, debris displacement, and biofilm disruption [19–25]. Er:YAG activation has also been studied with EDTA in extracted teeth [26, 27]. These tooth-based findings provide clinical motivation, but they do not make a two-dimensional bubble descriptor measured in an unconfined liquid a direct measure of cleaning or dentine safety.

The irrigant is part of the laser–liquid system rather than an inert carrier. Solutes in water-based endodontic preparations can change Er:YAG primary-bubble behaviour [28]. A separate comparison of eight endodontic irrigants found liquid-dependent optical-breakdown characteristics and laser-induced plasma activation (LIPA) bubble dynamics; in that experiment's 50-mJ condition, EDTA produced larger and longer-lived bubbles than distilled water [29]. That evidence supplies a specific reason to characterize EDTA directly instead of transferring numerical expectations from water. It did not, however, compare Er:YAG pulse modes or establish how a primary cavity couples to its first rebound in EDTA.

The 2025 conference abstract introduced LIPA for endodontic irrigation [30]. The multi-irrigant study established that LIPA breakdown and bubble dynamics depend on the liquid but included neither USP nor SSP [29], whereas the subsequent water study compared LIPA with USP but included no SSP or EDTA dataset [31]. Plasma-mediated Nd:YAG optical breakdown and thermally driven Er:YAG activation identify distinct primary-bubble initiation pathways [31–40]. These labels do not establish persistent plasma, pure vapour in a rebound, or absence of heating during LIPA. "Laser-generated bubbles" is the neutral category used here.

The objective was to characterize primary-to-first-rebound profiles across nine plasma-mediated Nd:YAG and thermally driven Er:YAG configurations in one tested unconfined 17% EDTA preparation. Within this two-family framework, focused ultra-short-pulse (USP) versus super-short-pulse (SSP) contrasts and an Er:YAG-only 2 × 3 analysis assessed complete device mode, shared pulse-energy setting and their interaction. LIPA supplied a non-energy-matched configuration reference, not a controlled test of initiation mechanism. Interpretation was restricted to image-resolved geometry and timing.

Materials and methods

Experimental design and laser activation

Experiments were performed in a 5 × 5 × 5-cm quartz cuvette with 1-mm JGS123 infrared-grade fused-silica walls (ZoParon Optical, China), three-quarters filled with nominal 17% EDTA (Longly Biotechnology, Wuhan, China). The formulation was the same as that reported in the multi-irrigant study [29]. Room temperature was 25°C, and a thermometer confirmed solution temperature of 25.0 ± 0.5°C immediately before each event. The cuvette platform, acquisition hardware, synchronization, calibration, and image-analysis workflow followed a published protocol [31]; study-specific elements are described below.

The matrix contained LIPA pulse energies of 100, 200, and 300 mJ per pulse and USP and SSP pulse energies of 10, 15, and 20 mJ (Figs. 1–2). Ten isolated-bubble events per configuration were analysed; no prospective sample-size calculation was documented. The 90 independent events were collected in randomized order, and same-setting USP and SSP samples were unpaired.

Plasma-mediated LIPA used a Q-switched 1064-nm Nd:YAG laser (LA-PULSAR300; MicroVec, Beijing, China) at pulse energies of 100, 200, or 300 mJ, 15 Hz, and 10 ns (0.010 μs). A 50-mm lens focused the approximately 8-mm

horizontal beam (2-mrad full-angle divergence) through the cuvette wall, 2.5 cm from the sidewall. The geometrically estimated focal scale was approximately 100 μm; in-liquid beam properties and deposited energy were not measured.

Thermally driven Er:YAG activation used a LightWalker M002-6A/2 laser (2940 nm; Fotona d.o.o., Ljubljana, Slovenia), H-14N handpiece, and a published tip geometry [31]. The vertical flat-ended tip (Flat SWEEPS 400/14; REF 84827) was 14 mm long, 0.4 mm in diameter, and immersed 5 mm. USP and SSP used pulse durations of 25 μs (0.025 ms) and 50 μs (0.050 ms) at 10, 15, or 20 mJ and 15 Hz (66.7-ms interpulse period). Pulse energy, waveform, and pulse-train stability, including the first pulse after activation, were measured with an Ophir Vega energy meter coupled to a pyroelectric energy sensor and verified with an oscilloscope and wavelength-matched silicon and InAsSb photodetectors, following the instrumentation arrangement [31]. Liquid-deposited energy was not measured.

High-speed acquisition and event alignment

For LIPA, the laser and high-speed camera shared a trigger signal. Because the Er:YAG console offered no external timing signal, image capture began before pulse initiation; a single pulse was then released through an electrically isolated footswitch circuit. Er:YAG timing was assigned from the recorded image sequence rather than from console latency.

Backlit 12-bit grayscale sequences were recorded at 50,000 frames/s (20 μs per frame) with an exposure of 1/900,000 s using a FASTCAM NOVA S20 camera (Photron), Laowa 100-mm 2× macro lens, and 200-W LUMINOR200A LED source (MicroVec). Display t = 0 was LIPA plasma luminescence or the first identifiable tip-associated USP/SSP bubble; the preceding Er:YAG frame (− 20 μs) was baseline. These were display origins, not a shared nucleation instant; quantitative intervals began at the first segmentable contour.

One separately supplied current-study sequence per configuration provided an illustrative primary-maximum frame (Fig. 1). Selection-only contour review did not contribute pixel-area or mask-derived quantitative endpoints. LIPA display frames used an identical full-field 8-bit linear mapping from 0–127 to 0–255, without new clipping or local masking; Er:YAG display levels were unchanged. LIPA source frames were unrotated. The supplied Er:YAG camera frames were rotated 90° clockwise for display, giving a vertical tip axis. This presentation operation was separate from the orientation of the exported analytical coordinates described below.

Spatial calibration converted image pixel dimensions to real physical dimensions before image processing. The calibrated images were evaluated frame by frame in MicroVec v3.6.5 using a published particle-size workflow [31]. All events were evaluated by one trained analyst; contour detection and Size export used fixed software settings, and no mask-derived endpoints were used. Numerical detection thresholds and event-specific calibration uncertainty were not available in the current records. For each oscillation, onset was the first segmentable contour, maximum the selected greatest-Size frame, and collapse the exported terminal-contour stage before re-expansion. These are sampled stages, not mathematical extrema between frames. Axial followed beam propagation and transverse was perpendicular. In the coordinate system underlying the exported Hor/Ver measurements, axial was horizontal for LIPA and vertical for USP/SSP. The supplied six-stage summaries, not the illustrative photographs, supported primary and rebound quantification.

Size-derived endpoints and data quality

Projected area was taken exclusively from the software-exported ellipse-equivalent projected-area descriptor Size, in square millimetres (Table 1). For every event stage, Size satisfied

Table 1
Primary-to-first-rebound descriptive profiles

Configuration	Size (mm²): P / R	Equivalent diameter (mm): P / R	Time to maximum (µs): P / R	Lifetime (µs): P / R	Rebound/primary diameter ratio	Primary axial rate (mm/ms)	Primary transverse rate (mm/ms)
LIPA 100 mJ	P: 10.117 [8.842, 11.490] R: 4.568 [3.487, 5.500]	P: 3.589 [3.355, 3.825] R: 2.411 [2.107, 2.646]	P: 160.0 [140.0, 160.0] R: 80 [65, 80]	P: 330.0 [300.0, 360.0] R: 160 [145, 180]	0.649 [0.619, 0.740]	11.024 [9.997, 11.752]	13.109 [12.483, 13.614]
LIPA 200 mJ	P: 23.991 [22.632, 25.427] R: 10.995 [9.528, 11.508]	P: 5.527 [5.368, 5.690] R: 3.742 [3.482, 3.828]	P: 240.0 [220.0, 260.0] R: 140 [120, 155]	P: 500.0 [480.0, 500.0] R: 310 [280, 320]	0.657 [0.639, 0.690]	9.811 [8.458, 10.845]	14.425 [13.056, 16.431]
LIPA 300 mJ	P: 24.651 [22.293, 33.085] R: 11.449 [9.168, 16.509]	P: 5.601 [5.328, 6.487] R: 3.809 [3.416, 4.583]	P: 240.0 [225.0, 260.0] R: 140 [125, 160]	P: 500.0 [465.0, 585.0] R: 290 [260, 390]	0.690 [0.644, 0.711]	9.119 [8.013, 9.923]	14.919 [13.333, 15.844]
USP 10 mJ	P: 4.310 [4.001, 4.480] R: 2.520 [2.436, 2.675]	P: 2.342 [2.257, 2.388] R: 1.791 [1.761, 1.845]	P: 140.0 [120.0, 140.0] R: 80 [80, 80]	P: 280.0 [265.0, 280.0] R: 160 [160, 160]	0.775 [0.768, 0.794]	10.064 [9.727, 11.790]	9.769 [9.095, 11.811]
USP 15 mJ	P: 5.450 [5.335, 5.698] R: 2.995 [2.850, 3.267]	P: 2.634 [2.606, 2.694] R: 1.953 [1.905, 2.039]	P: 160.0 [140.0, 160.0] R: 90 [80, 100]	P: 320.0 [305.0, 320.0] R: 180 [180, 180]	0.750 [0.731, 0.755]	10.369 [9.708, 10.819]	9.758 [8.698, 10.500]
USP 20 mJ	P: 6.513 [6.453, 6.634] R: 3.540	P: 2.880 [2.866, 2.906] R: 2.123 [2.115, 2.149]	P: 160.0 [160.0, 160.0] R: 80 [60, 80]	P: 340.0 [340.0, 340.0] R: 200 [200, 200]	0.737 [0.723, 0.753]	9.690 [9.289, 10.071]	9.227 [8.216, 10.255]

*Note. * Median [Q1, Q3]; n = 10 independent events per configuration. P = primary; R = first rebound, always in that line order. Size is the software-exported ellipse-equivalent projected area; equivalent diameter = 2√(Size/π), so these are not independent geometric measurements. The diameter ratio is calculated within each event before summarizing. Acquisition is 20 µs/frame; median intervals such as 30 or 90 µs do not imply finer sampling. Rates are signed finite-interval projected full-length changes, not interface or fluid velocities. Plasma-mediated LIPA is not energy matched to thermally driven USP/SSP.*

Configuration	Size (mm²): P / R	Equivalent diameter (mm): P / R	Time to maximum (µs): P / R	Lifetime (µs): P / R	Rebound/primary diameter ratio	Primary axial rate (mm/ms)	Primary transverse rate (mm/ms)
	[3.512, 3.626]						
SSP 10 mJ	P: 2.883 [2.838, 2.967] R: 1.150 [1.090, 1.204]	P: 1.916 [1.901, 1.944] R: 1.210 [1.178, 1.238]	P: 100.0 [100.0, 100.0] R: 60 [60, 60]	P: 220.0 [220.0, 220.0] R: 120 [120, 120]	0.629 [0.616, 0.650]	9.506 [9.196, 10.965]	9.255 [8.732, 12.380]
SSP 15 mJ	P: 3.594 [3.397, 3.740] R: 1.297 [1.166, 1.348]	P: 2.139 [2.080, 2.182] R: 1.285 [1.218, 1.310]	P: 100.0 [100.0, 100.0] R: 40 [25, 40]	P: 240.0 [240.0, 255.0] R: 120 [120, 120]	0.587 [0.575, 0.606]	11.259 [10.758, 12.998]	13.912 [12.881, 16.565]
SSP 20 mJ	P: 4.090 [3.918, 4.257] R: 1.139 [1.017, 1.260]	P: 2.282 [2.233, 2.328] R: 1.204 [1.138, 1.267]	P: 100.0 [100.0, 120.0] R: 30 [20, 40]	P: 260.0 [245.0, 260.0] R: 100 [85, 100]	0.535 [0.509, 0.549]	9.845 [9.255, 11.446]	13.126 [11.996, 16.093]

*Note. * Median [Q1, Q3]; n = 10 independent events per configuration. P = primary; R = first rebound, always in that line order. Size is the software-exported ellipse-equivalent projected area; equivalent diameter = 2√(Size/π), so these are not independent geometric measurements. The diameter ratio is calculated within each event before summarizing. Acquisition is 20 µs/frame; median intervals such as 30 or 90 µs do not imply finer sampling. Rates are signed finite-interval projected full-length changes, not interface or fluid velocities. Plasma-mediated LIPA is not energy matched to thermally driven USP/SSP.*

$$A = \pi L_{ax} L_{tr}/4,$$

where L_{ax} and L_{tr} are the beam-referenced full axial and transverse lengths. Equivalent circular diameter was the deterministic transform

$$D_{eq} = 2\sqrt{(A/\pi)} = \sqrt{(L_{ax} L_{tr})}.$$

Area and diameter encode the same orthogonal-length geometry and were not counted as independent evidence. The Size identity does not establish that the observed contour is elliptical or document MicroVec's fitting algorithm. The rebound index, $D_{eq,rebound}/D_{eq,primary}$, equals the square root of the rebound/primary area ratio and is geometric, not an energy-retention estimate.

Time to maximum ran from the first segmentable contour to the maximum-Size frame; lifetime ended at terminal collapse. Although the worksheet header said milliseconds, the authors confirmed 50,000-frame/s acquisition and microsecond timestamps; every stage and interval also passed the 20-µs grid audit. Directional rates were recomputed from stage measurements. For each axis,

v_app = [L(t_Amax) − L(t_onset)]/[(t_Amax − t_onset)/1000],

where t is in μs and L is the corresponding axial or transverse full length. Division by 1000 converts the interval to ms; rates are reported in mm/ms (numerically m/s). Because the maximum-Size frame need not maximize an axis, this signed apparent full-length rate can be negative. It is an interval-averaged projected-length change, not an instantaneous interface, shock, or fluid-flow velocity. Aspect ratio was L_ax/L_tr.

The principal reporting family comprised primary maximum D_eq, primary axial and transverse rates, first-rebound maximum D_eq, and rebound/primary diameter ratio. Areas were companion descriptors; timing, lengths, aspect ratios and rebound rates were secondary. Identifier, stage, time-grid, geometry and rate checks identified no missing principal outcome or nonpositive interval in the final 540-stage, 90-event dataset. All supplied events entered analysis; the source package did not enumerate candidate acquisitions outside this set. No second-analyst or test–retest subset was processed for the current dataset, and reliability coefficients were not obtained; the checks above are bookkeeping audits and do not substitute for measurement repeatability.

Statistical analysis

Continuous outcomes are median [Q1–Q3]. Each of the five principal outcomes underwent a nine-configuration Kruskal–Wallis test, with Holm adjustment across the family (Table 2); eligible outcomes were followed by all 36 two-sided, tie-corrected Mann–Whitney comparisons, Holm adjusted within outcome. Rank tests assess distributional ordering, not exclusively median differences when distributional shapes differ. Cliff’s delta and same-setting USP-minus-SSP median differences were summarized with event-level percentile bootstrap intervals, and principal omnibus results were checked by Monte Carlo permutation.

Table 2
Complete omnibus, factorial and ordered-setting inference

Outcome / family	Omnibus H; Holm-5 p	Mode F; Holm-15 p	Setting F; Holm-15 p	Mode × setting F; Holm-15 p	LIPA trend JT; Holm-15 p	USP trend JT; Holm-15 p	SSP trend JT; Holm-15 p
Primary equivalent diameter (principal)	H = 85.752 p = 1.688e-14	F = 673.744 p = 0.000150	F = 162.713 p = 0.000150	F = 7.030 p = 0.009420	JT = 260.0 p = 0.000300	JT = 295.0 p = 0.000300	JT = 288.0 p = 0.000300
Primary axial rate (principal)	H = 13.572 p = 0.093636	F = 0.770 p = 0.412396	F = 2.073 p = 0.372716	F = 1.520 p = 0.412396	JT = 94.5 p = 0.209636	JT = 125.0 p = 1.000000	JT = 150.0 p = 1.000000
Primary transverse rate (principal)	H = 47.562 p = 2.396e-07	F = 22.171 p = 0.000150	F = 2.348 p = 0.372716	F = 3.435 p = 0.174798	JT = 208.5 p = 0.183116	JT = 125.0 p = 1.000000	JT = 210.0 p = 0.178716
Rebound equivalent diameter (principal)	H = 82.773 p = 5.399e-14	F = 1378.332 p = 0.000150	F = 23.348 p = 0.000150	F = 26.318 p = 0.000150	JT = 253.0 p = 0.000400	JT = 281.0 p = 0.000300	JT = 147.0 p = 1.000000
Rebound/primary diameter ratio (principal)	H = 67.205 p = 5.297e-11	F = 430.088 p = 0.000150	F = 24.145 p = 0.000150	F = 8.162 p = 0.003570	JT = 164.0 p = 1.000000	JT = 88.0 p = 0.170817	JT = 21.0 p = 0.000300
Rebound time to maximum (exploratory secondary)	H = 72.378 p = 6.035e-12	—	—	—	—	—	—
Rebound lifetime (exploratory secondary)	H = 72.572 p = 6.035e-12	—	—	—	—	—	—
Rebound axial rate (exploratory secondary)	H = 56.339 p = 4.845e-09	—	—	—	—	—	—
Rebound transverse rate (exploratory secondary)	H = 36.033 p = 1.732e-05	—	—	—	—	—	—

*Note. * Principal and exploratory-secondary omnibus rows are two separate five-outcome Holm families (Kruskal–Wallis, N = 90, df = 8), not one ten-test adjustment. Omnibus p values are asymptotic. The Er:YAG-only 2 × 3 factorial analysis uses approximate HC3-studentized Freedman–Lane residual permutation (N = 60; 100,000 permutations; mode df = 1, setting/interaction df = 2, reference error df = 54), with Holm across all 15 terms. ART is a complementary rank-scale check, not an identical estimand. All 15 original two-sided Jonckheere–Terpstra tests (50,000 permutations) retain their original Holm-15 correction. Setting order is 100/200/300 mJ for LIPA and 10/15/20 mJ for USP/SSP. — means outside the specified factorial/trend reporting family, not a nonsignificant result. No primary-rate trend survived adjustment.*

Outcome / family	Omnibus H; Holm-5 p	Mode F; Holm-15 p	Setting F; Holm-15 p	Mode × setting F; Holm-15 p	LIPA trend JT; Holm-15 p	USP trend JT; Holm-15 p	SSP trend JT; Holm-15 p
Rebound aspect ratio (exploratory secondary)	H = 79.255 p = 3.452e-13	—	—	—	—	—	—

*Note. * Principal and exploratory-secondary omnibus rows are two separate five-outcome Holm families (Kruskal–Wallis, N = 90, df = 8), not one ten-test adjustment. Omnibus p values are asymptotic. The Er:YAG-only 2 × 3 factorial analysis uses approximate HC3-studentized Freedman–Lane residual permutation (N = 60; 100,000 permutations; mode df = 1, setting/interaction df = 2, reference error df = 54), with Holm across all 15 terms. ART is a complementary rank-scale check, not an identical estimand. All 15 original two-sided Jonckheere–Terpstra tests (50,000 permutations) retain their original Holm-15 correction. Setting order is 100/200/300 mJ for LIPA and 10/15/20 mJ for USP/SSP. — means outside the specified factorial/trend reporting family, not a nonsignificant result. No primary-rate trend survived adjustment.*

The six Er:YAG cells formed a balanced 2 × 3 analysis (mode × pulse-energy setting; N = 60), using reduced-model residual permutation following Freedman and Lane [41] with an HC3-studentized Wald F statistic on the raw additive scale; all 15 term tests were Holm adjusted together (Table 2). This supporting factorial inference is approximate under heterogeneous variances, and its additive-scale mean contrasts differ from the descriptive median contrasts. Aligned-rank-transform models [42] in IBM SPSS Statistics 27 provided complementary rank-scale sensitivity checks, and independent software cross-checks compared endpoint summaries and test outputs.

The rebound extension was post hoc and exploratory. Ordered-setting Jonckheere–Terpstra tests were Holm adjusted across all 15 principal-outcome-by-mode tests (Table 2). The five rebound secondary outcomes formed a separate Kruskal–Wallis Holm family, and their same-setting USP–SSP contrasts retained within-outcome Holm-36 correction (Tables 2 and 3). Within-event shape change, ln (rebound aspect/primary aspect), was evaluated by exact two-sided signed-rank tests with Holm-9 adjustment; exactness is conditional on a symmetric-about-zero null distribution of paired log changes. All intervals are marginal, not multiplicity-adjusted; adjusted two-sided $p < 0.05$ governed inference. No analysis was preregistered.

Table 3
Complete focused independent USP–SSP comparisons

Outcome / family	10 mJ	15 mJ	20 mJ
Primary equivalent diameter (mm) (principal)	Δ = 0.427 [0.323, 0.500] δ = 1.000; p = 0.005590	Δ = 0.495 [0.423, 0.613] δ = 1.000; p = 0.005590	Δ = 0.598 [0.542, 0.671] δ = 1.000; p = 0.005590
Primary transverse rate (mm/ms) (principal)	Δ = 0.514 [-3.486, 2.928] δ = 0.000; p = 1.000000	Δ = -4.154 [-7.457, -2.358] δ = -0.900; p = 0.020568	Δ = -3.899 [-7.708, -1.760] δ = -0.800; p = 0.059701
Rebound equivalent diameter (mm) (principal)	Δ = 0.581 [0.528, 0.657] δ = 1.000; p = 0.005654	Δ = 0.668 [0.599, 0.792] δ = 1.000; p = 0.005654	Δ = 0.919 [0.844, 1.002] δ = 1.000; p = 0.005654
Rebound/primary diameter ratio (dimensionless) (principal)	Δ = 0.146 [0.110, 0.174] δ = 1.000; p = 0.005654	Δ = 0.163 [0.126, 0.182] δ = 1.000; p = 0.005654	Δ = 0.202 [0.179, 0.238] δ = 1.000; p = 0.005654
Rebound time to maximum (exploratory secondary)	δ = 0.84 p = 0.011473	δ = 0.96 p = 0.004555	δ = 1.00 p = 0.003572
Rebound lifetime (exploratory secondary)	δ = 0.99 p = 0.002482	δ = 0.80 p = 0.016246	δ = 0.91 p = 0.007293
Rebound axial rate (exploratory secondary)	δ = 0.43 p = 1.000000	δ = 0.12 p = 1.000000	δ = 0.42 p = 1.000000
Rebound transverse rate (exploratory secondary)	δ = 0.87 p = 0.032114	δ = -0.16 p = 1.000000	δ = 0.36 p = 1.000000
Rebound aspect ratio (exploratory secondary)	δ = -0.98 p = 0.005654	δ = -1.00 p = 0.005654	δ = -1.00 p = 0.005654

*Note. * All 12 principal-outcome and 15 exploratory-secondary comparisons are shown. Principal cells give USP-minus-SSP median difference Δ [marginal 95% bootstrap CI], Cliff's δ and p; Δ has the stated outcome unit. Secondary cells give δ and p. δ is oriented USP minus SSP. All two-sided tie-corrected asymptotic Mann–Whitney p values retain the original Holm correction across 36 pairs separately within each outcome, not across the 27 displayed comparisons. Median-difference CIs use 50,000 independent within-group bootstrap resamples and are not multiplicity adjusted. Group medians for principal outcomes are in* Table 1. *Nonsignificant contrasts are retained; absent primary axial-rate contrasts were not part of the original eligible focused principal set. Primary timing contrasts (time to maximum and lifetime at each of the three settings) are summarized in the text; all six retained within-outcome Holm-36 significance (adjusted p ≤ 0.0025). Group medians for the rebound-rate contrasts are given in the Results text.*

Results

Shared-setting thermally driven USP–SSP profiles

At 10, 15 and 20 mJ, USP primary-area medians were 4.310, 5.450 and 6.513 mm², compared with 2.883, 3.594 and 4.090 mm² for SSP (Table 1). Corresponding equivalent-diameter medians were 2.342, 2.634 and 2.880 mm for USP and 1.916, 2.139 and 2.282 mm for SSP (Fig. 3a). The descriptive USP-minus-SSP median-area difference therefore widened from 1.427 to 2.423 mm².

First-rebound area medians were 2.520, 2.995 and 3.540 mm² for USP, versus 1.150, 1.297 and 1.139 mm² for SSP. Rebound-diameter medians were 1.791, 1.953 and 2.123 mm versus 1.210, 1.285 and 1.204 mm (Fig. 3c); USP-minus-SSP median differences were 0.581, 0.668 and 0.919 mm. Rebound/primary diameter ratios were 0.775,

0.750 and 0.737 for USP versus 0.629, 0.587 and 0.535 for SSP (Fig. 3d). All observed USP values exceeded all same-setting SSP values for primary area/diameter, rebound area/diameter and the ratio (sample Cliff's δ = 1.00; within-outcome Holm-36 p ≤ 0.0057; Table 3). This sample separation does not establish non-overlap of the populations.

USP primary time-to-maximum medians were 140, 160 and 160 µs versus 100 µs at each SSP setting; primary lifetimes were 280, 320 and 340 µs versus 220, 240 and 260 µs. All six same-setting comparisons remained significant (adjusted p ≤ 0.0025). Rebound lifetimes were 160, 180 and 200 µs for USP and 120, 120 and 100 µs for SSP: median differences of 40, 60 and 100 µs (Holm-36 p = 0.00248, 0.01625 and 0.00729). Rebound time-to-maximum medians were 80, 90 and 80 µs for USP versus 60, 40 and 30 µs for SSP (adjusted p ≤ 0.0115; Tables 1 and 3).

Supporting factorial, directional and LIPA results

Approximate Er:YAG factorial tests identified mode, setting and interaction associations for primary diameter, rebound diameter and rebound ratio; interaction Holm-15 p values were 0.00942, 0.000150 and 0.00357 (Table 2). No axial-rate term was significant. Transverse rate showed a mode association (adjusted p = 0.000150), but not a setting or interaction association (p = 0.373 and 0.175). SSP exceeded USP at 15 mJ (13.912 versus 9.758 mm/ms; Holm-36 p = 0.0206), while the 20-mJ difference was not significant after correction (p = 0.0597; Fig. 4; Table 3).

In the supporting nine-configuration panorama, primary diameter, transverse rate, rebound diameter and rebound ratio differed (all Holm-5 p < 0.001), whereas axial rate did not (p = 0.094; Table 2). Plasma-mediated LIPA primary-area medians were 10.117, 23.991 and 24.651 mm², and rebound areas were 4.568, 10.995 and 11.449 mm². These external-reference measurements were not energy matched to Er:YAG. All five exploratory rebound-secondary omnibus outcomes differed (Table 2). However, no same-setting USP–SSP rebound axial-rate contrast survived correction (all p = 1.000). Rebound transverse rate was higher for USP only at 10 mJ (14.325 versus 9.702 mm/ms; p = 0.0321); the 15/20-mJ contrasts were not significant after adjustment (both p = 1.000; Table 3).

Exploratory absolute and relative rebound responses

Rebound diameter showed ordered increases across LIPA and USP settings (Holm-15 trend p = 0.000400 and 0.000300), but no ordered increase was detected for SSP (p = 1.000; Table 2). From 10 to 20 mJ, SSP primary-area medians increased by 41.9%, while rebound-area medians changed from 1.150 to 1.139 mm². The rebound-diameter median difference was − 0.005 mm from unrounded values (marginal 95% bootstrap interval, − 0.089 to 0.071 mm; Holm-36 p = 0.811), a descriptive difference within expected single-analyst measurement variability; this is not an equivalence or plateau result.

SSP's rebound/primary diameter ratio declined from 0.629 to 0.535 (Holm-15 trend p = 0.000300). USP's smaller descriptive decline, from 0.775 to 0.737, did not survive adjustment (p = 0.171); no ordered ratio trend was detected for LIPA (p = 1.000). Absolute and relative rebound size therefore provided different descriptions of the setting response.

Exploratory rebound anisotropy and paired shape change

All 30 LIPA rebound projections had axial/transverse aspect ratios above one, whereas all 30 USP projections had ratios below one (Fig. 5a; Table 4). SSP had 10/10 ratios below one at 10 mJ, seven below and three above one at 15 mJ, and 10/10 above one at 20 mJ. SSP aspect-ratio medians were 0.831, 0.906 and 1.167; the 20-versus-10-mJ comparison retained significance (Holm-36 p = 0.00565). This within-SSP comparison is not a between-mode interaction test.

Table 4
Exploratory within-event primary-to-rebound shape change

Configuration	Rebound aspect median [Q1, Q3]	Rebound aspect > 1 (n/10)	Median log change [95% CI]	Rank-biserial effect	Exact Holm-9 p
LIPA 100 mJ	1.459 [1.408, 1.554]	10/10	0.384 [0.273, 0.415]	1.000	0.017578
LIPA 200 mJ	1.388 [1.329, 1.466]	10/10	0.192 [0.106, 0.357]	1.000	0.017578
LIPA 300 mJ	1.240 [1.193, 1.293]	10/10	0.123 [0.061, 0.176]	0.709	0.097656
USP 10 mJ	0.574 [0.553, 0.659]	0/10	-0.618 [-0.658, -0.450]	-1.000	0.017578
USP 15 mJ	0.645 [0.626, 0.689]	0/10	-0.486 [-0.560, -0.408]	-1.000	0.017578
USP 20 mJ	0.674 [0.642, 0.711]	0/10	-0.401 [-0.474, -0.330]	-1.000	0.017578
SSP 10 mJ	0.831 [0.785, 0.894]	0/10	-0.201 [-0.284, -0.089]	-1.000	0.017578
SSP 15 mJ	0.906 [0.855, 1.009]	3/10	-0.019 [-0.121, 0.126]	-0.018	1.000000
SSP 20 mJ	1.167 [1.090, 1.420]	10/10	0.351 [0.258, 0.563]	1.000	0.017578

*Note. * Aspect = axial/transverse length at the respective maximum-Size frame. Log change = ln(rebound aspect/primary aspect), paired within an event. Exact two-sided sign-flip signed-rank tests enumerate all 2^10 assignments; Holm across all nine groups. CIs are marginal paired bootstrap 95% intervals, not multiplicity-adjusted. Positive change means a shift toward axial elongation; negative means a shift toward transverse elongation. Exact signed-rank inference assumes a symmetric-zero distribution of within-event log-aspect differences; enumeration does not make the test assumption-free. Seven configurations had W = 0 and raw p = 0.001953125; LIPA300 had W = 8 and p = 0.048828125; SSP15 had W = 27 and p = 1.*

Paired log-aspect changes supported relative axial shifts in LIPA100/200 and SSP20, and transverse shifts in all USP groups and SSP10 (Holm-9 p = 0.01758 each; Fig. 5b). Each of these seven configurations had all ten changes in the stated direction. LIPA300, with nine positive changes, and SSP15 did not meet the adjusted criterion (p = 0.09766 and 1.000). A positive paired shift and an absolute aspect ratio above one are distinct descriptors. These quantitative results derive from the stage dataset; Fig. 1 illustrates primary maxima only.

Discussion

The nine configurations showed distinct primary-to-first-rebound profiles across plasma-mediated Nd:YAG and thermally driven Er:YAG activation in one tested 17% EDTA preparation. USP produced larger primary and rebound

projections, higher rebound/primary diameter ratios and longer timing intervals at every shared setting. The exploratory extension showed that absolute rebound size, relative size and projected anisotropy need not respond together. LIPA occupied a larger absolute-size range but was not energy matched to Er:YAG. Neither this difference nor projected shape isolates the initiating pathway as its cause.

EDTA is clinically relevant because of its chelating role in smear-layer management [1–5], but the cuvette contained no dentine or mineral substrate. Solute-dependent Er:YAG bubble behaviour [28] and the multi-irrigant LIPA findings [29] justify characterizing this preparation directly rather than transferring numerical expectations from water. Liquid composition was not a randomized factor here. The absence of pH, viscosity, surface-tension, density, additive and gas-content measurements does not permit attribution of mode differences to any individual property; the findings concern the tested preparation.

The first rebound was not simply represented by one common primary-to-rebound scale factor. In SSP, primary-area medians increased across settings while the low/high rebound-area medians remained close—a descriptive difference within expected measurement variability—and the relative rebound diameter declined. USP showed increasing absolute rebound size, but its ratio trend was not significant after adjustment. Because primary size is the ratio's denominator, the decline must be interpreted alongside the absolute rebound measurement; it is not independent evidence of greater energy loss. Collapse and rebound depend on deformation, compressibility, boundaries and shock emission [43–45], but none of those contributions was measured separately.

Projected anisotropy added a descriptor that equivalent diameter cannot supply. The sampled LIPA rebounds were axially dominant and USP rebounds transversely dominant; SSP shifted from predominantly transverse to axial projections across its tested settings. Paired shape changes distinguish an oscillation-to-oscillation shift from the absolute rebound aspect ratio. Their exploratory status, n = 10 per configuration and symmetric-null assumption require caution. Each significant configuration depended on unanimity of all ten paired changes; single-event sign reversals within measurement variability would alter the adjusted results. Hard classifications around aspect ratio one is sensitive to measurement uncertainty; some SSP20 values approached that boundary. No jet direction, three-dimensional shape or wall loading can be inferred from these orthogonal projected lengths.

Area and diameter remain deterministic representations of the same Size geometry, not independent confirmations. Likewise, a finite-interval full-length rate need not track equivalent-diameter growth because the maximum-Size frame need not maximize either axis. The nonsignificant axial findings do not establish equivalence. Sampling at 20 μs particularly limits short rebound intervals: medians such as 30 or 90 μs arise from averaging central observations, not finer acquisition. Neither apparent rate nor a rebound-size ratio estimates pressure, fluid transport or retained energy.

The factorial associations support setting-dependent complete-mode differences on the raw additive scale but are not isolated pulse-duration effects. Delivered pulse energy, waveform, and pulse-train stability were measured as described above; liquid-deposited energy and tip peak power were not measured. Variance heterogeneity and small cells also limit residual-permutation inference, despite HC3 studentization. Rank-scale sensitivity agreement and software cross-checks improve computational transparency without removing these assumptions. The direct same-setting sample contrasts remain the clearest evidence.

The three earlier outputs provide premise and methodological continuity rather than reused results: the IDJ abstract introduced LIPA [30], the PPLS article examined multiple irrigants without USP/SSP [29], and the LIMS water study compared LIPA with USP but included neither SSP nor the current EDTA dataset [31]. The authors confirmed no

overlapping events, frames or derived data. The present contribution is the within-EDTA, two-family configuration comparison, including SSP and exploratory primary-to-rebound shape changes. It does not estimate an EDTA-versus-water effect.

Several limitations constrain translation. The cuvette lacked canal anatomy, apical resistance and dentine, although tip, free-surface and wall boundaries remained [17, 20–24]. The preparation was characterized only by supplier and nominal concentration, and acquisition records covered the analysed set rather than the wider candidate history. All 540 stages were processed by a single trained analyst without a second-analyst or test–retest subset, so reliability coefficients cannot be reported. No pressure, flow, irrigant-exchange or biological endpoint was measured; confined-model studies combining imaging with transport or pressure measurements are the next step.

Conclusion

Plasma-mediated Nd:YAG and thermally driven Er:YAG configurations exhibited different primary-to-rebound profiles in one unconfined 17% EDTA preparation. Same-setting USP produced larger primary and first-rebound projections, higher rebound/primary diameter ratios and longer timing intervals than SSP. SSP primary enlargement was not accompanied by a comparable change in absolute rebound size. Exploratory paired analysis identified projected-shape shifts that differed across the tested configurations and warrant independent confirmation. LIPA remained a non-energy-matched reference; family labels describe initiation, not rebound composition. These findings provide a preparation-specific physical baseline for subsequent confined-canal studies, without establishing an EDTA-versus-water effect, energy retention, pressure safety or clinical efficacy.

Declarations

Author Contribution

Y.B.: conceptualization, methodology, investigation, formal analysis, writing – original draft. R.W.: methodology, investigation. L.T.: investigation, formal analysis. Y.Z.: supervision, project administration, writing – review and editing. All authors reviewed the manuscript.

Acknowledgement

The authors thank the technical team of MicroVec Ltd. (Beijing, China) for assistance with the high-speed imaging setup, synchronization and consultation on the image-analysis software.

Data Availability

The datasets generated and analyzed during the present study are available from the corresponding author on reasonable request.

References

1. Boutsioukis C, Arias-Moliz MT (2022) Present status and future directions—irrigants and irrigation methods. Int Endod J 55(Suppl 3):588–612. https://doi.org/10.1111/iej.13739
2. Zehnder M (2006) Root canal irrigants. J Endod 32:389–398. https://doi.org/10.1016/j.joen.2005.09.014

3. Hülsmann M, Heckendorff M, Lennon Á (2003) Chelating agents in root canal treatment: mode of action and indications for their use. Int Endod J 36:810–830. https://doi.org/10.1111/j.1365-2591.2003.00754.x
4. Violich DR, Chandler NP (2010) The smear layer in endodontics—a review. Int Endod J 43:2–15. https://doi.org/10.1111/j.1365-2591.2009.01627.x
5. Calt S, Serper A (2002) Time-dependent effects of EDTA on dentin structures. J Endod 28:17–19. https://doi.org/10.1097/00004770-200201000-00004
6. Siqueira JF, Rôças IN (2022) Present status and future directions: Microbiology of endodontic infections. Int Endod J 55(Suppl 3):512–530. https://doi.org/10.1111/iej.13677
7. Vertucci FJ (2005) Root canal morphology and its relationship to endodontic procedures. Endod Top 10:3–29. https://doi.org/10.1111/j.1601-1546.2005.00129.x
8. Versiani M, Martins J, Ordinola-Zapata R (2023) Anatomical complexities affecting root canal preparation: a narrative review. Aust Dent J 68:S5–S23. https://doi.org/10.1111/adj.12992
9. Meire M, De Moor RJG (2024) Principle and antimicrobial efficacy of laser-activated irrigation: a narrative review. Int Endod J 57:841–860. https://doi.org/10.1111/iej.14042
10. De Groot SD, Verhaagen B, Versluis M, Wu MK, Wesselink PR, Van Der Sluis LWM (2009) Laser-activated irrigation within root canals: cleaning efficacy and flow visualization. Int Endod J 42:1077–1083. https://doi.org/10.1111/j.1365-2591.2009.01634.x
11. Blanken J, De Moor RJG, Meire M, Verdaasdonk R (2009) Laser induced explosive vapor and cavitation resulting in effective irrigation of the root canal. Part 1: a visualization study. Lasers Surg Med 41:514–519. https://doi.org/10.1002/lsm.20798
12. Matsumoto H, Yoshimine Y, Akamine A (2011) Visualization of irrigant flow and cavitation induced by Er:YAG laser within a root canal model. J Endod 37:839–843. https://doi.org/10.1016/j.joen.2011.02.035
13. Mrochen M, Riedel P, Donitzky C, Seiler T (2001) Erbium:yttrium–aluminum–garnet laser induced vapor bubbles as a function of the quartz fiber tip geometry. J Biomed Opt 6:344–350. https://doi.org/10.1117/1.1381052
14. Gregorčič P, Jezeršek M, Možina J (2012) Optodynamic energy-conversion efficiency during an Er:YAG-laser-pulse delivery into a liquid through different fiber-tip geometries. J Biomed Opt 17:075006. https://doi.org/10.1117/1.JBO.17.7.075006
15. Lukac N, Zadravec J, Gregorcic P, Lukac M, Jezeršek M (2016) Wavelength dependence of photon-induced photoacoustic streaming technique for root canal irrigation. J Biomed Opt 21:075007. https://doi.org/10.1117/1.JBO.21.7.075007
16. Lukač N, Gregorčič P, Jezeršek M (2016) Optodynamic phenomena during laser-activated irrigation within root canals. Int J Thermophys 37:66. https://doi.org/10.1007/s10765-016-2071-z
17. Lukač N, Jezeršek M (2018) Amplification of pressure waves in laser-assisted endodontics with synchronized delivery of Er:YAG laser pulses. Lasers Med Sci 33:823–833. https://doi.org/10.1007/s10103-017-2435-z
18. Lukač M, Lukač N, Jezeršek M (2020) Characteristics of bubble oscillations during laser-activated irrigation of root canals and method of improvement. Lasers Surg Med 52:907–915. https://doi.org/10.1002/lsm.23226
19. Kouno A, Watanabe S, Hongo T, Yao K, Satake K, Okiji T (2020) Effect of pulse energy, pulse frequency, and tip diameter on intracanal vaporized bubble kinetics and apical pressure during laser-activated irrigation using Er:YAG laser. Photobiomodul Photomed Laser Surg 38:431–437. https://doi.org/10.1089/photob.2019.4739
20. Jezeršek M, Lukač N, Lukač M, Tenyi A, Olivi G, Fidler A (2020) Measurement of pressures generated in root canal during Er:YAG laser-activated irrigation. Photobiomodul Photomed Laser Surg 38:625–631. https://doi.org/10.1089/photob.2019.4776

21. Jezeršek M, Lukač N, Lukač M (2021) Measurement of simulated debris removal rates in an artificial root canal to optimize laser-activated irrigation parameters. Lasers Surg Med 53:411–417. https://doi.org/10.1002/lsm.23297
22. Swimberghe RCD, Tzourmanas R, De Moor RJG, Braeckmans K, Coenye T, Meire MA (2022) Explaining the working mechanism of laser-activated irrigation and its action on microbial biofilms: a high-speed imaging study. Int Endod J 55:1372–1384. https://doi.org/10.1111/iej.13824
23. Nagahashi T, Yahata Y, Handa K, Nakano M, Suzuki S, Kakiuchi Y, Tanaka T, Kanehira M, Suresh Venkataiah V, Saito M (2022) Er:YAG laser-induced cavitation can activate irrigation for the removal of intraradicular biofilm. Sci Rep 12:4897. https://doi.org/10.1038/s41598-022-08963-x
24. Li Z, Su Z, Liu H, Bai Y, Shen Y, Pan C (2024) Phase-locked μPIV analysis of flow dynamics in a simulated root canal with different laser-activated irrigations. Lasers Med Sci 39:112. https://doi.org/10.1007/s10103-024-04051-w
25. Bürklein S, Abdi I, Schäfer E, Appel C, Donnermeyer D (2024) Influence of pulse energy, tip design and insertion depth during Er:YAG-activated irrigation on cleaning efficacy in simulated severely curved complex root canal systems in vitro. Int Endod J 57:87–99. https://doi.org/10.1111/iej.13992
26. DiVito E, Peters OA, Olivi G (2012) Effectiveness of the erbium:YAG laser and new design radial and stripped tips in removing the smear layer after root canal instrumentation. Lasers Med Sci 27:273–280. https://doi.org/10.1007/s10103-010-0858-x
27. Sahar-Helft S, Pinto N, Dakar A, Helft C, Steinberg D, Mayer Y (2026) Er:YAG laser-activated 17% EDTA with side-firing tip preserves root canal dentin integrity: a micro-CT study. Lasers Med Sci 41:15. https://doi.org/10.1007/s10103-026-04800-z
28. Meire M, van Aelst B, Sehovic A, Deari S, Zehnder M (2024) Solutes in water affect the primary cavitation bubble generated by a pulsed erbium-doped yttrium aluminium garnet laser. Lasers Med Sci 39:298. https://doi.org/10.1007/s10103-024-04257-y
29. Bai Y, Wei R (2026) Comparative analysis of nanosecond pulsed Nd:YAG laser-induced cavitation bubbles in different endodontic irrigants with far-field focused irradiation. Photobiomodul Photomed Laser Surg 44:109–118. https://doi.org/10.1177/25785478251409030
30. Bai Y, Wei R, Zhao Y (2025) Laser-induced plasma activation: an innovation to enhance endodontic irrigation. Int Dent J 75:104799. https://doi.org/10.1016/j.identj.2025.104799
31. Bai Y, Zhao Y (2026) Comparative bubble dynamics of plasma-mediated Nd:YAG laser-induced optical breakdown and thermally driven Er:YAG laser-activated irrigation in water. Lasers Med Sci 41:199. https://doi.org/10.1007/s10103-026-04999-x
32. Linz N, Freidank S, Liang XX, Vogel A (2025) Laser-induced plasma formation and cavitation in water: from nanoeffects to extreme states of matter. Rep Prog Phys 88:088501. https://doi.org/10.1088/1361-6633/adedb3
33. Venugopalan V, Guerra A III, Nahen K, Vogel A (2002) Role of laser-induced plasma formation in pulsed cellular microsurgery and micromanipulation. Phys Rev Lett 88:078103. https://doi.org/10.1103/PhysRevLett.88.078103
34. Vogel A, Busch S, Parlitz U (1996) Shock wave emission and cavitation bubble generation by picosecond and nanosecond optical breakdown in water. J Acoust Soc Am 100:148–165. https://doi.org/10.1121/1.415878
35. Vogel A, Nahen K, Theisen D, Noack J (1996) Plasma formation in water by picosecond and nanosecond Nd:YAG laser pulses. I. Optical breakdown at threshold and superthreshold irradiance. IEEE J Sel Top Quantum

Electron 2:847–860. https://doi.org/10.1109/2944.577307

36. Vogel A, Noack J, Nahen K, Theisen D, Busch S, Parlitz U, Hammer DX, Noojin GD, Rockwell BA, Birngruber R (1999) Energy balance of optical breakdown in water at nanosecond to femtosecond time scales. Appl Phys B 68:271–280. https://doi.org/10.1007/s003400050617
37. Noack J, Vogel A (1999) Laser-induced plasma formation in water at nanosecond to femtosecond time scales: calculation of thresholds, absorption coefficients, and energy density. IEEE J Quantum Electron 35:1156–1167. https://doi.org/10.1109/3.777215
38. Quinto-Su PA, Venugopalan V, Ohl CD (2008) Generation of laser-induced cavitation bubbles with a digital hologram. Opt Express 16:18964–18969. https://doi.org/10.1364/OE.16.018964
39. Lim KY, Quinto-Su PA, Klaseboer E, Khoo BC, Venugopalan V, Ohl CD (2010) Nonspherical laser-induced cavitation bubbles. Phys Rev E 81:016308. https://doi.org/10.1103/PhysRevE.81.016308
40. Kennedy PK, Hammer DX, Rockwell BA (1997) Laser-induced breakdown in aqueous media. Prog Quantum Electron 21:155–248. https://doi.org/10.1016/S0079-6727(97)00002-5
41. Freedman D, Lane D (1983) A nonstochastic interpretation of reported significance levels. J Bus Econ Stat 1:292–298. https://doi.org/10.1080/07350015.1983.10509354
42. Wobbrock JO, Findlater L, Gergle D, Higgins JJ (2011) The aligned rank transform for nonparametric factorial analyses using only ANOVA procedures. In: Proceedings of the SIGCHI Conference on Human Factors in Computing Systems, pp 143–146. Association for Computing Machinery, New York. https://doi.org/10.1145/1978942.1978963
43. Liang XX, Linz N, Freidank S, Paltauf G, Vogel A (2022) Comprehensive analysis of spherical bubble oscillations and shock wave emission in laser-induced cavitation. J Fluid Mech 940:A5. https://doi.org/10.1017/jfm.2022.202
44. Akhatov I, Lindau O, Topolnikov A, Mettin R, Vakhitova N, Lauterborn W (2001) Collapse and rebound of a laser-induced cavitation bubble. Phys Fluids 13:2805–2819. https://doi.org/10.1063/1.1401810
45. Tinguely M, Obreschkow D, Kobel P, Dorsaz N, de Bosset A, Farhat M (2012) Energy partition at the collapse of spherical cavitation bubbles. Phys Rev E 86:046315. https://doi.org/10.1103/PhysRevE.86.046315

Figures

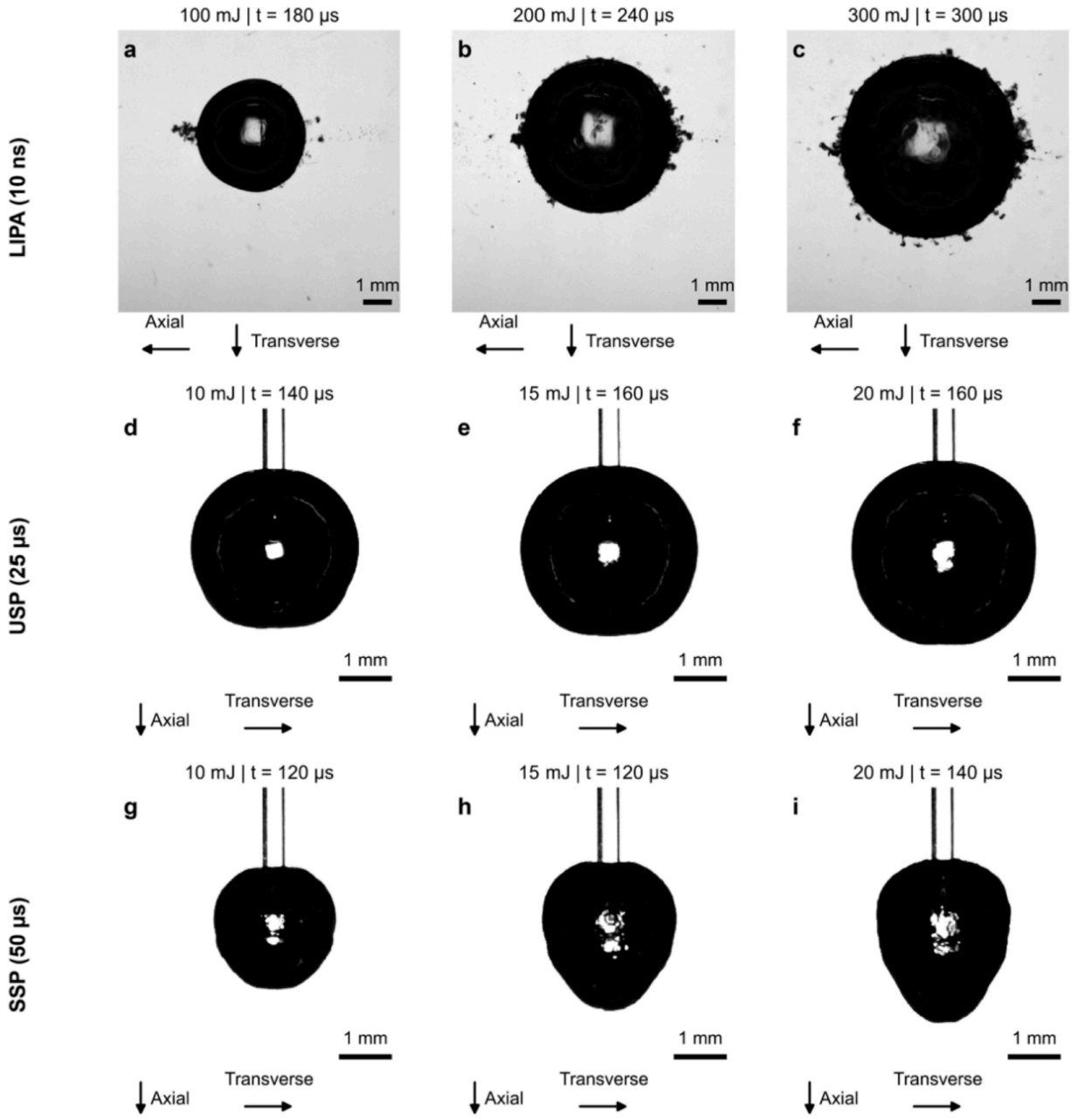


Figure 1

Representative primary-maximum frames in unconfined 17% EDTA. a–c Plasma-mediated Nd:YAG/LIPA at 100, 200 and 300 mJ (10 ns); d–f thermally driven Er:YAG/USP at 10, 15 and 20 mJ (25 µs); g–i thermally driven Er:YAG/SSP at 10, 15 and 20 mJ (50 µs). Acquisition was 50,000 frames/s (20 µs/frame). Following [31], t = 0 is LIPA plasma luminescence or the first identifiable Er:YAG tip-associated bubble. Each panel shows the largest primary projection from one illustrative sequence, not all 90 selections, and includes a modality-calibrated 1-mm bar; no rebound frame is shown. LIPA is unrotated (axial left, transverse down); Er:YAG is rotated 90° clockwise (axial down, transverse right). For display only, all LIPA frames shared a 0–127 to 0–255 linear mapping and all Er:YAG frames one linear gray rescaling. No local masking or artificial texture was added.

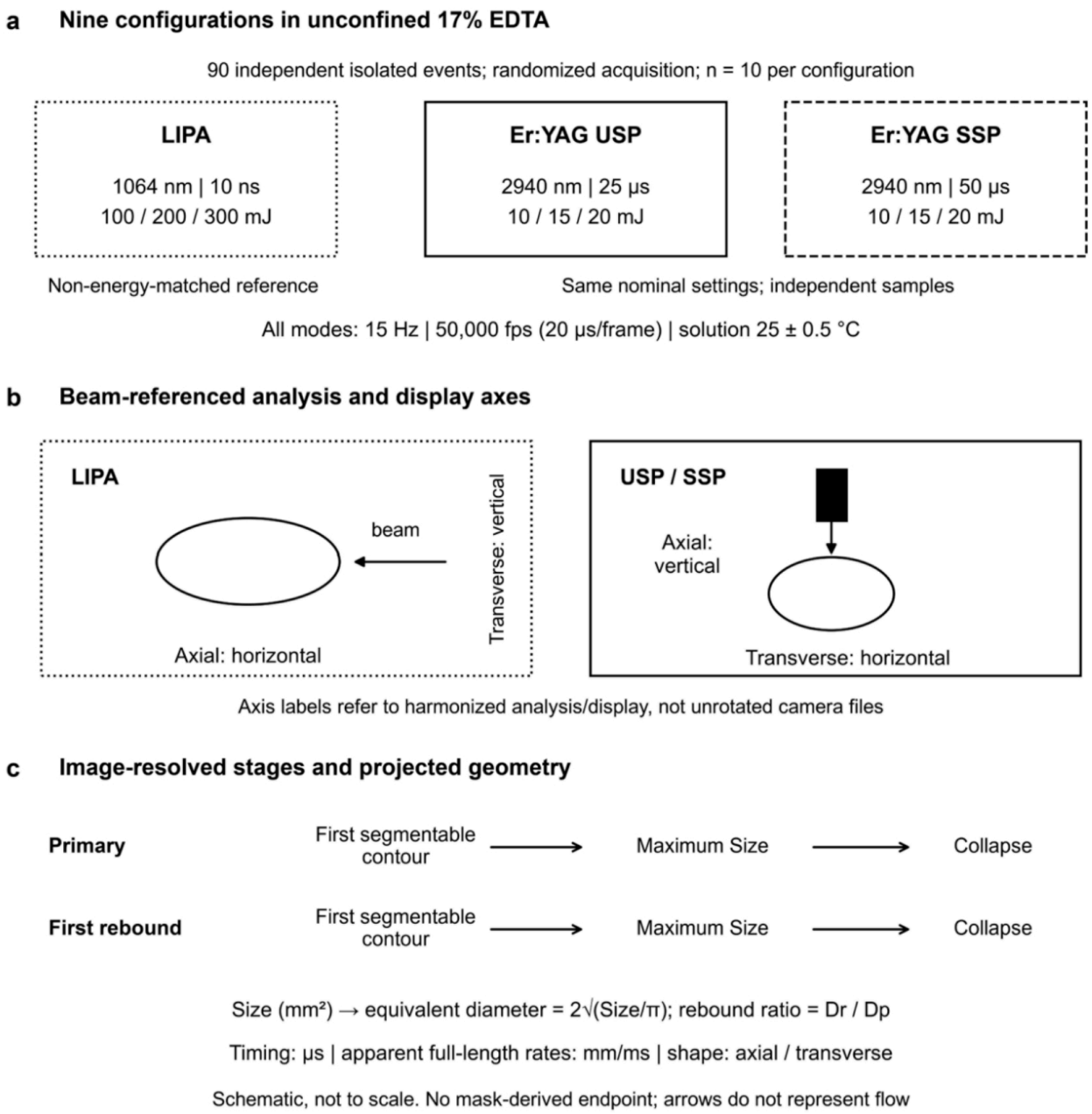


Figure 2

Configuration and measurement framework. a Nine configurations (n = 10 independent, randomly acquired isolated events each): LIPA 100/200/300 mJ, 10 ns; USP 10/15/20 mJ, 25 µs; SSP 10/15/20 mJ, 50 µs; all at 15 Hz. LIPA was a non-energy-matched reference. b Axial follows beam propagation and transverse is perpendicular; LIPA axial is horizontal, Er:YAG axial vertical, and the displayed LIPA beam travels right to left. Arrows do not indicate flow. c Primary and first-rebound stages and Size-derived endpoints; timing begins at the first segmentable contour. Schematics are not to scale.

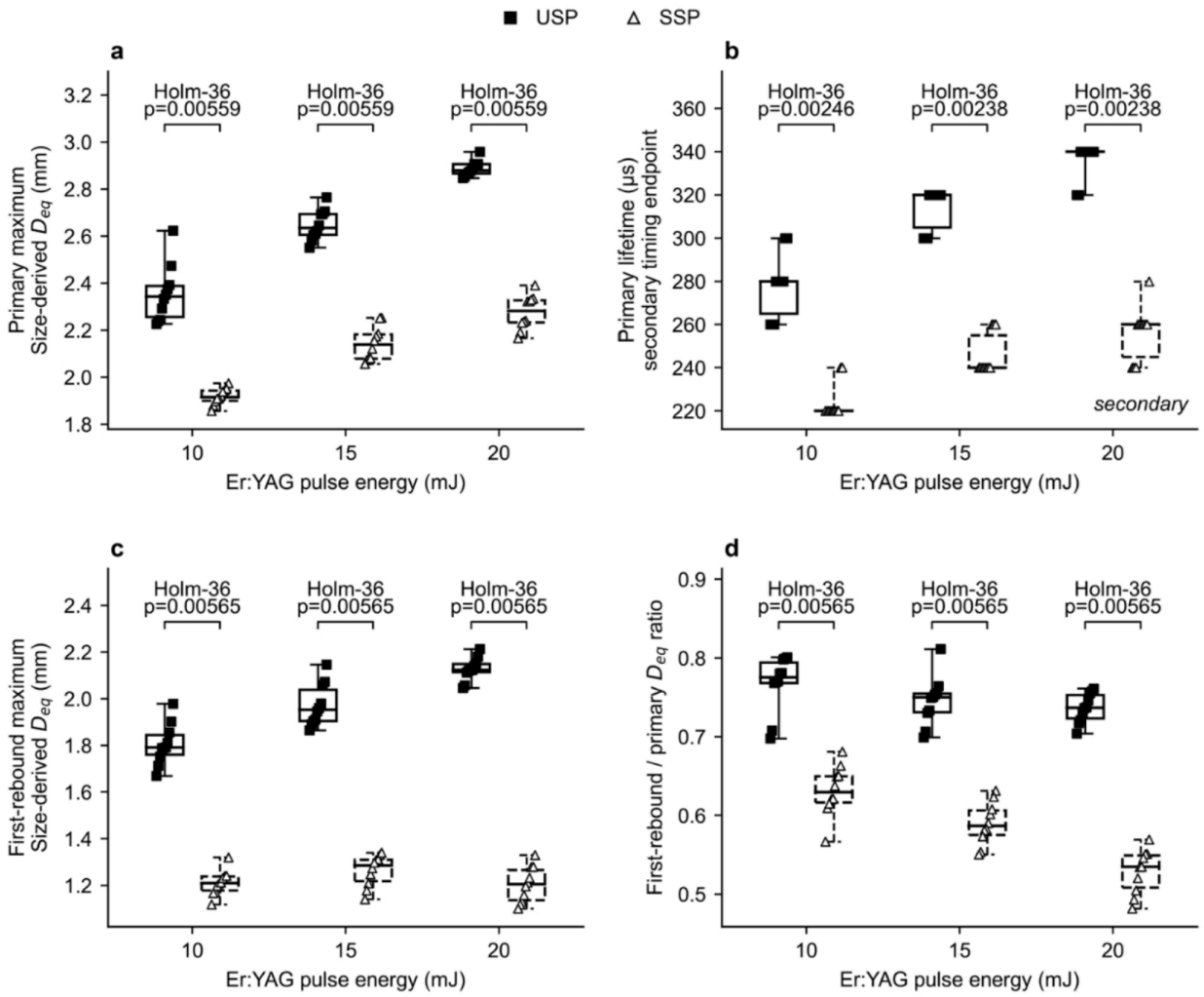
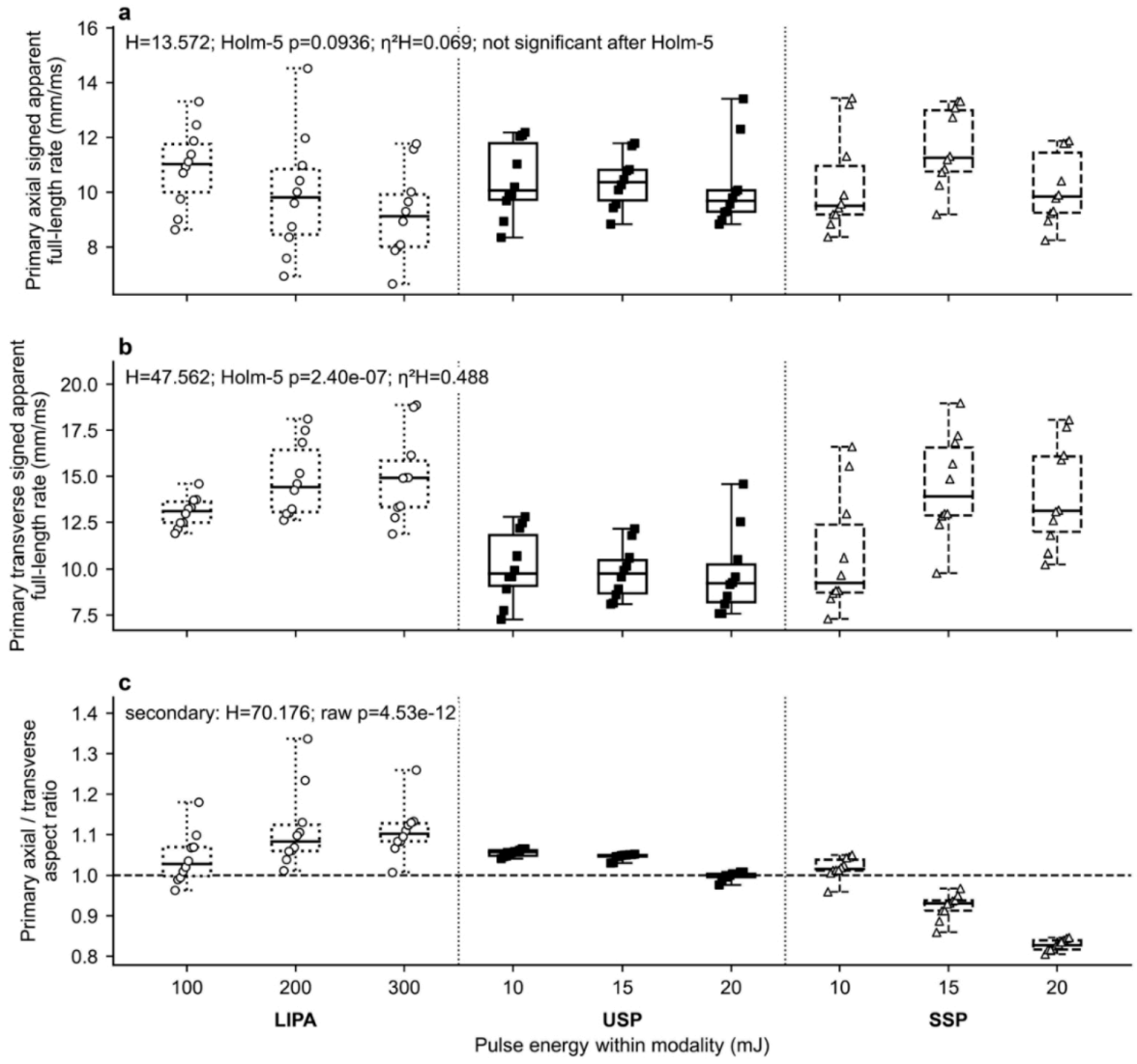


Figure 3

Primary-to-first-rebound distributions for thermally driven USP and SSP. a Primary-maximum Size-derived equivalent diameter; b primary lifetime; c rebound maximum equivalent diameter; d rebound/primary diameter ratio. All independent events are shown (n = 10 per mode/setting); same-setting groups are unpaired. Boxes show Q1–Q3, medians and observed ranges. Brackets give two-sided, tie-corrected asymptotic Mann–Whitney p values, Holm-adjusted across 36 comparisons. Filled squares/solid outlines denote USP; open triangles/dashed outlines denote SSP. Lifetime is secondary, and the diameter ratio is geometric rather than retained energy.



LIPA: axial = image horizontal; USP/SSP: axial = image vertical. LIPA is not energy matched to Er:YAG.

Figure 4

Primary directional descriptors across plasma-mediated LIPA and thermally driven USP/SSP. a Axial and b transverse signed apparent full-length rates; c axial/transverse aspect ratio. Rates are onset-to-maximum-Size length changes, not instantaneous interface, shock or fluid velocities; the maximum-Size frame need not maximize either axis. Each configuration contains ten independent events. Boxplot conventions follow Fig. 3; open circles/dotted outlines denote LIPA, filled squares/solid outlines USP and open triangles/dashed outlines SSP. For a and b, $\eta^2_H = (H - k + 1)/(N - k)$, with $k = 9$ and $N = 90$. Axes are beam referenced; the aspect-ratio annotation is an unadjusted secondary omnibus result.

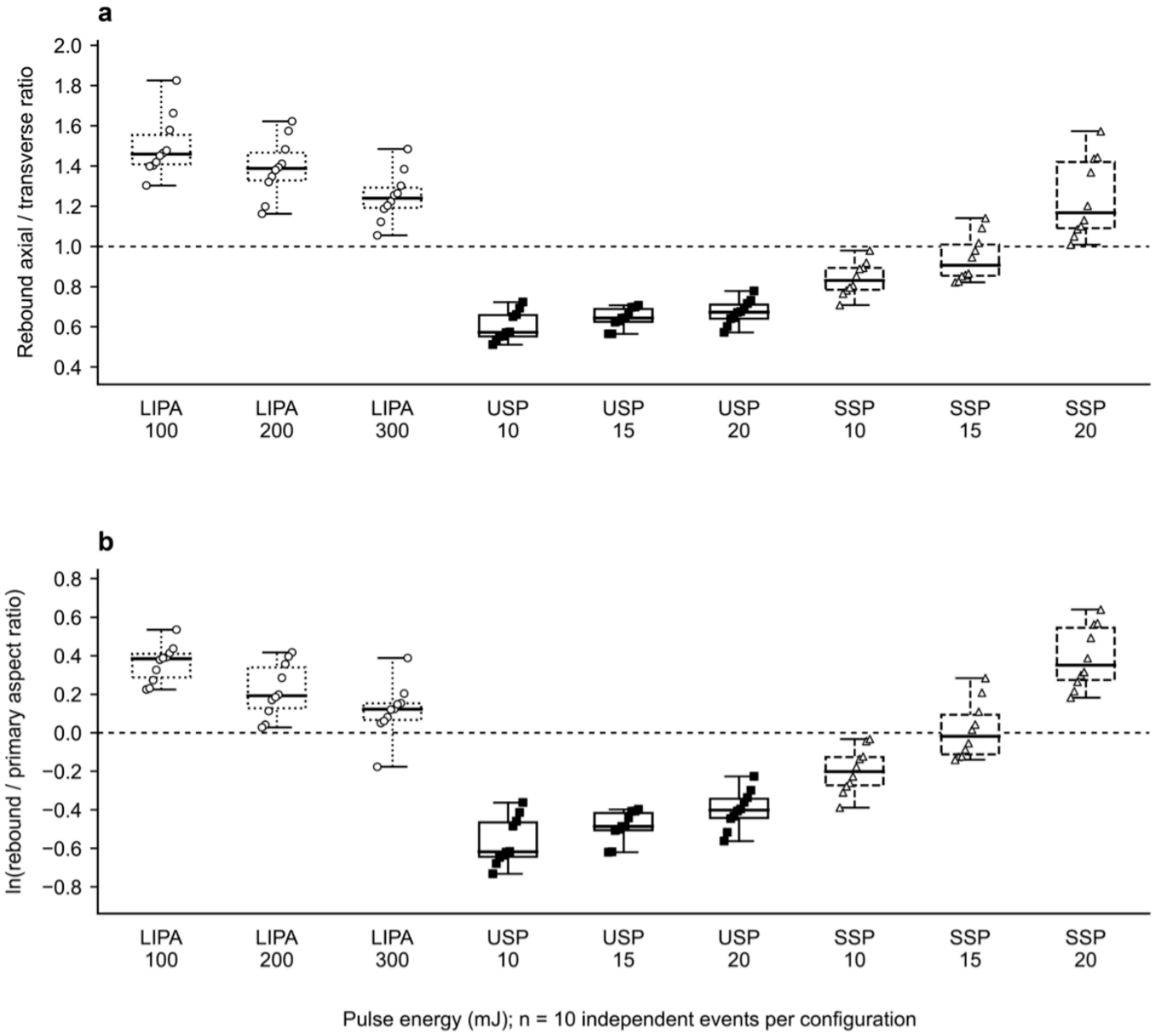


Figure 5

Exploratory rebound anisotropy and paired shape change after plasma-mediated LIPA or thermally driven USP/SSP initiation. a Rebound axial/transverse aspect ratio at maximum rebound Size; the reference line denotes equal lengths. b Within-event ln(rebound aspect/primary aspect); zero denotes no change. All 90 events are shown; conventions follow Figs. 3–4. Exact signed-rank tests assume a symmetric zero-centred null and are Holm-adjusted across nine configurations (Table 4). These two-dimensional projections do not establish rebound morphology, three-dimensional shape or jet direction.